

UV-dropout Galaxies in the GOODS-South Field from WFC3 Early Release Science Observations

N. P. Hathi¹, R. E. Ryan Jr.², S. H. Cohen³, H. Yan⁴, R. A. Windhorst³, P. J. McCarthy⁵, R. W. O'Connell⁶, A. M. Koekemoer⁷, M. J. Rutkowski³, B. Balick⁸, H. E. Bond⁷, D. Calzetti⁹, M. J. Disney¹⁰, M. A. Dopita¹¹, Jay A. Frogel¹², D. N. B. Hall¹³, J. A. Holtzman¹⁴, R. A. Kimble¹⁵, F. Paresce¹⁶, A. Saha¹⁷, J. I. Silk¹⁸, J. T. Trauger¹⁹, A. R. Walker²⁰, B. C. Whitmore⁷, and E. T. Young²¹

Nimish.Hathi@ucr.edu

ABSTRACT

¹Department of Physics and Astronomy, University of California, Riverside, CA 92521

²Department of Physics and Astronomy, University of California, Davis, CA 92616

³School of Earth and Space Exploration, Arizona State University, Tempe, AZ 85287-1404

⁴Center for Cosmology and AstroParticle Physics, The Ohio State University, Columbus, OH 43210

⁵Observatories of the Carnegie Institute of Washington, Pasadena, CA 91101, USA

⁶Department of Astronomy, University of Virginia, Charlottesville, VA 22904-4325

⁷Space Telescope Science Institute, Baltimore, MD 21218

⁸Department of Astronomy, University of Washington, Seattle, WA 98195-1580

⁹Department of Astronomy, University of Massachusetts, Amherst, MA 01003

¹⁰School of Physics and Astronomy, Cardiff University, Cardiff CF24 3AA, United Kingdom

¹¹Research School of Astronomy & Astrophysics, The Australian National University, ACT 2611, Australia

¹²Association of Universities for Research in Astronomy, Washington, DC 20005

¹³Institute for Astronomy, University of Hawaii, Honolulu, HI 96822

¹⁴Department of Astronomy, New Mexico State University, Las Cruces, NM 88003

¹⁵NASA-Goddard Space Flight Center, Greenbelt, MD 20771

¹⁶Istituto di Astrofisica Spaziale e Fisica Cosmica, INAF, Via Gobetti 101, 40129 Bologna, Italy

¹⁷National Optical Astronomy Observatories, Tucson, AZ 85726-6732

¹⁸Department of Physics, University of Oxford, Oxford OX1 3PU, United Kingdom

¹⁹NASA-Jet Propulsion Laboratory, Pasadena, CA 91109

²⁰Cerro Tololo Inter-American Observatory, La Serena, Chile

²¹NASA-Ames Research Center, Moffett Field, CA 94035

We combine new high sensitivity ultraviolet (UV) imaging from the Wide Field Camera 3 (WFC3) on the Hubble Space Telescope (HST) with existing deep HST/Advanced Camera for Surveys (ACS) optical images from the Great Observatories Origins Deep Survey (GOODS) program to identify UV-dropouts, which are Lyman break galaxy (LBG) candidates at $z \simeq 1-3$. These new HST/WFC3 observations were taken over 50 arcmin² in the GOODS-South field as a part of the Early Release Science program. The uniqueness of these new UV data is that they are observed in 3 UV/optical (WFC3 UVIS) channel filters (F225W, F275W and F336W), which allows us to identify three different sets of UV-dropout samples. We apply Lyman break dropout selection criteria to identify F225W-, F275W- and F336W-dropouts, which are $z \simeq 1.7$, 2.1 and 2.7 LBG candidates, respectively. We use multi-wavelength imaging combined with available spectroscopic and photometric redshifts to carefully access the validity of our UV-dropout candidates. Our results are as follows: (1) these WFC3 UVIS filters are very reliable in selecting LBGs with $z \simeq 2.0$, which helps to reduce the gap between the well studied $z \gtrsim 3$ and $z \sim 0$ regimes; (2) the combined number counts with average redshift $z \simeq 2.2$ agrees very well with the observed change in the surface densities as a function of redshift when compared with the higher redshift LBG samples; and (3) the best-fit Schechter function parameters from the rest-frame UV luminosity functions at three different redshifts fit very well with the evolutionary trend of the characteristic absolute magnitude, M^* , and the faint-end slope, α , as a function of redshift. This is the first study to illustrate the usefulness of the WFC3 UVIS channel observations to select $z \lesssim 3$ LBGs. The addition of the new WFC3 on the HST has made it possible to uniformly select LBGs from $z \simeq 1$ to $z \simeq 9$, and significantly enhance our understanding of these galaxies using HST sensitivity and resolution.

Subject headings: galaxies: high redshift — galaxies:luminosity function, mass function — galaxies:evolution

1. Introduction

The Lyman break ‘dropout’ technique was first applied to select Lyman break galaxies (LBGs) at $z \simeq 3$ (Guhathakurta et al. 1990; Steidel et al. 1996, 1999), and since then it has been extensively used to select LBG candidates at $z \simeq 3-9$ (e.g., Sawicki & Thompson 2006; Bouwens et al. 2007; Reddy et al. 2008; Rafelski et al. 2009; Oesch et al. 2010; Bunker et al. 2010; Yan et al. 2010). This dropout technique has generated large samples of star-bursting

galaxy candidates at $z \simeq 3 - 9$, but there is only one major study (Ly et al. 2009) that investigates LBGs at $z \simeq 1 - 3$ based on dropout selection criteria. The primary reason for this is that we need highly sensitive space-based cameras to observe the mid- to near-ultraviolet (UV) wavelengths required to select LBGs at $z \simeq 1 - 3$. The new Wide Field Camera 3 (WFC3) on the refurbished Hubble Space Telescope (HST) with its superior sensitivity — compared to the Wide-Field Planetary Camera 2 (WFPC2) or the Galaxy Evolution Explorer (GALEX) — and filters below the atmospheric cut-off wavelength (e.g., F225W and F275W), allows us to photometrically identify and study lower redshift ($z \simeq 1 - 3$) LBGs. The improved sensitivity/depth allows us to probe the lower luminosity systems at these redshifts.

There are two important reasons to understand these LBGs. First, to study the star formation properties of these LBGs, because they are at redshifts corresponding to the peak epoch of the global star formation rate (e.g., Ly et al. 2009; Bouwens et al. 2010a,b; Yan et al. 2010), and, secondly, they are likely lower redshift analogs of the high redshift LBGs — because of the similar dropout selection at all redshifts — whose understanding will help shed light on the process of reionization in the early Universe (e.g., Labb   et al. 2010; Stark et al. 2010; Yan et al. 2010). The major advantage of identifying and studying various properties — including star formation properties — of lower redshift LBGs is that these LBGs can be investigated in rest-frame UV *as well as* rest-frame optical filters. The high redshift LBGs have very little information on their rest-frame *optical* properties, so a detailed understanding of lower redshift LBGs is very important to get insight into the physical and morphological nature of high redshift LBGs.

The new UV observations of the WFC3 Science Oversight Committee (SOC) Early Release Science extragalactic program (PID: 11359, PI: O’Connell; hereafter “ERS2”), covers approximately 50 arcmin² in the north-western part of the Great Observatories Origins Deep Survey (GOODS; Giavalisco et al. 2004a) South field. Here we use the high sensitivity of the new WFC3 UVIS channel data, along with existing deep optical data obtained with the Advanced Camera for Surveys (ACS) as part of the GOODS program, to search for LBG candidates at $z \simeq 1 - 3$. We use dropout color selection criteria based on color-color plots, obtained with the WFC3 UVIS and ACS filters to find three unique sets of UV dropouts — F225W-dropouts, F275W-dropouts and F336W-dropouts — which are LBG candidates at $z \simeq 1.7, 2.1$ and 2.7 , respectively (as shown in Figure 1).

This paper is organized as follows: In § 2 we summarize the WFC3 ERS2 observations, and in § 2.1 we discuss the selection, and in § 2.2 the reliability of our color selected $z \simeq 1 - 3$ LBG sample. In § 3 we discuss the data analysis, which includes measuring their number counts and surface density (§ 3.1), and compare these with other surveys at higher redshifts,

and estimate rest-frame UV luminosity functions (§ 3.2) for these samples. In § 4 we conclude with a summary of our results.

In the remaining sections of this paper we refer to the HST/WFC3 F225W, F275W, F336W, filters as U_{225} , U_{275} , U_{336} , and HST/ACS F435W, F606W, F775W, F850LP filters as B_{435} , V_{606} , i_{775} , z_{850} , respectively, for convenience. We assume a *Wilkinson Microwave Anisotropy Probe* (WMAP) cosmology with $\Omega_m=0.274$, $\Omega_\Lambda=0.726$ and $H_0=70.5 \text{ km s}^{-1} \text{ Mpc}^{-1}$, in accord with the 5 year WMAP estimates of Komatsu et al. (2009). This corresponds to a look-back time of 10.37 Gyr at $z\simeq 2$. Magnitudes are given in the AB_v system (Oke & Gunn 1983).

2. Observations

The WFC3 ERS2 observations were done in both the UVIS (with a FOV of 7.30 arcmin²) and the IR (with a FOV of 4.65 arcmin²) channels. Details of these observations are described in Windhorst et al. (2010). Here we briefly summarize the UV imaging observations. The WFC3 ERS2 UV observations were done in three broad-band filters U_{225} , U_{275} and U_{336} , whose total throughput curves are shown in Figure 1. The ERS2 field covers the north-western ~ 50 arcmin² of the GOODS-South field, and was observed in 8 pointings with a 2×4 grid pattern during September-October 2009. The U_{225} and U_{275} filters were observed for 2 orbits per pointing, while the U_{336} filter was observed for 1 orbit per pointing, for a total of 40 orbits over the full ERS2 field. The raw images were processed through the CALWF3 task (using the latest version as of December 1, 2009) included in the STSDAS package (version 3.11), and the latest reference files from the STScI. The flat-fielded images were then aligned and drizzled using MULTIDRIZZLE (Koekemoer et al. 2002) onto the same grid as the GOODS-South v2.0¹ ACS data, which were rebinned to a pixel size of 0.09''. The final UV image mosaics have a pixel scale of 0.09'' — to match the WFC3 IR image mosaics — in all filters, and cover ~ 50 arcmin² area in the GOODS-South field.

The combination of the three WFC3 UV filters and the four ACS optical filters provide excellent capability of selecting galaxies at $z\simeq 1-3$, using the dropout technique to detect the Lyman-break signature that occurs at a rest-frame wavelength of 912 Å (Madau 1995). Figure 1 shows the locations of the rest-frame 912 Å Lyman break at various redshifts. It is clear that three WFC3 UVIS filters, along with the ACS B_{435} - and V_{606} -bands are very useful in identifying LBG candidates at $z\simeq 1-3$. We performed matched-aperture photometry by running the SExtractor (Bertin & Arnouts 1996) algorithm in the dual-image mode with the

¹<http://archive.stsci.edu/pub/hlsp/goods/v2/>

corresponding RMS maps. The RMS maps were derived from the MULTIDRIZZLE generated weight maps, following the procedure discussed in Dickinson et al. (2004). We have measured the 10σ point source detection limits in a $0.2''$ aperture as 26.0, 26.1 and 25.7 AB-mag in U_{225} , U_{275} and U_{336} , respectively. We constructed three separate catalogs by using the three separate images (U_{275} , U_{336} , B_{435}) as detection images. These catalogs are referred as the U_{275} -based, U_{336} -based and B_{435} -based catalogs. We used the WFC3 in-flight photometric zeropoints (24.06, 24.14, 24.64 AB-mag for U_{225} , U_{275} & U_{336} ; Kalirai et al. 2009) obtained from STScI website².

2.1. Color Selection

Our initial selection of UV dropouts is based on dropout color criteria obtained from the stellar population models of Bruzual & Charlot (2003, BC03). The top three panels of Figure 2 shows the BC03 star-forming galaxy models for three dropout samples with $E(B - V) = 0, 0.15, 0.30$ mag (solid black lines), expected colors of stars (black dots) from Pickles (1998), and tracks of low-redshift ellipticals (gray lines) from Kinney et al. (1996) and Coleman et al. (1980). The gray shaded region in top panels is our selection region. Though Galactic stars clearly land in the selection region in Figure 2, these are easily removed by simple morphological criteria, as in Windhorst et al. (2010). We have applied the Madau (1995) prescription to estimate IGM attenuation for proper comparison with other studies. We also checked how BC03 tracks are affected by applying the Madau prescription only to galaxies at $z > 2.5$ (i.e. no IGM attenuation below $z < 2.5$), and only to galaxies at $z > 1.0$, to see the effects of fluctuations in IGM attenuation. We find that our adopted selection criteria will still be able to pick-up star-forming galaxies with $E(B - V) < 0.3$. The selection criteria adopted here are similar to the criteria used to identify LBG candidates at $z \simeq 3-8$ (e.g., Steidel et al. 1996; Giavalisco et al. 2004b; Bouwens et al. 2010a,b; Yan et al. 2010). We use U_{275} -based catalogs to select U_{225} -dropouts using $(U_{225} - U_{275})$ vs. $(U_{275} - U_{336})$ color-color space, as shown in the bottom leftmost panel of Figure 2. For U_{225} -band dropouts, we require:

$$\left\{ \begin{array}{l} (U_{225} - U_{275}) > 1.3 \text{ mag and } U_{275} \leq 26.5 \text{ mag} \\ \text{and } (U_{275} - U_{336}) < 1.2 \text{ mag} \\ \text{and } (U_{275} - U_{336}) > -0.2 \text{ mag} \\ \text{and } (U_{225} - U_{275}) > 0.35 + [1.3 \times (U_{275} - U_{336})] \text{ mag} \\ \text{and } (U_{336} - B_{435}) > -0.5, [S/N(U_{275})] > 3, [S/N(U_{225})] < 3 \end{array} \right.$$

²zeropoints were made public in September 2009: http://www.stsci.edu/hst/wfc3/phot_zp_lbn/

Here, the S/N is defined as 1.0857 divided by the **SExtractor** error in the total magnitude. The **SExtractor** magnitude uncertainties are estimated from carefully constructed RMS maps that account for correlated pixel noise and hence, gives better estimate of the noise. Details of the WFC3 data reduction process are given in Windhorst et al. (2010). We require $(U_{225} - U_{275}) > 1.3$ mag, which is redder than what we have applied for other dropouts, because there is no bluer filter available than U_{225} to confirm that these dropouts are undetected at wavelengths bluer than rest-frame 912 Å. We have also applied the additional criterion $(U_{336} - B_{435}) > -0.5$ mag to eliminate the possibility of selecting spurious candidates, since this color-color space is based only on three UV filters, and it is required that LBG candidates be detected and are bright enough in the B_{435} -band. The B_{435} -band is about $\sim 2\text{--}2.5$ mag deeper than the U_{336} -band, so a simple $S/N (B_{435}) > 3$ cut cannot be used, because we would still pick-up very faint objects in B_{435} -band. There are 106 objects inside the selection region. We find a total of 70 LBG candidates (U_{225} -dropouts) based on these selection criteria. After visually checking each candidate using the 10-band (3 WFC3 UV, 4 ACS optical and 3 WFC3 IR) HST imaging from the ERS2 GOODS observations, we eliminated 4 candidates from our sample as spurious (due to their closeness to a bright object or a probable faint stellar diffraction spike). This examination leaves us with 66 U_{225} -dropouts.

Similarly, we use U_{336} -based catalogs to select U_{275} -dropouts using $(U_{275} - U_{336})$ vs. $(U_{336} - B_{435})$ color-color space as shown in the bottom middle panel of Figure 2. For U_{275} -band dropouts, we require:

$$\left\{ \begin{array}{l} (U_{275} - U_{336}) > 1.0 \text{ mag and } U_{336} \leq 26.5 \text{ mag} \\ \text{and } (U_{336} - B_{435}) < 1.2 \text{ mag} \\ \text{and } (U_{336} - B_{435}) > -0.2 \text{ mag} \\ \text{and } (U_{275} - U_{336}) > 0.35 + [1.3 \times (U_{336} - B_{435})] \text{ mag} \\ \text{and } [S/N(U_{336})] > 3, [S/N(U_{275})] < 3, [S/N(U_{225})] < 1 \end{array} \right.$$

There are 223 objects inside the selection region. We find a total of 153 LBG candidates (U_{275} -dropouts) based on these selection criteria. After visual examination, we eliminated 2 candidates from our sample as spurious, because of their proximity to a brighter object. Therefore, our core sample contains 151 U_{275} -dropouts.

Finally, we use B_{435} -based catalogs to select U_{336} -dropouts using $(U_{336} - B_{435})$ vs. $(B_{435} - V_{606})$ color-color space as shown in the bottom rightmost panel of Figure 2. For U_{336} -band

dropouts, the following color selection was applied:

$$\left\{ \begin{array}{l} (U_{336} - B_{435}) > 0.8 \text{ mag and } B_{435} \leq 26.5 \text{ mag} \\ \text{and } (B_{435} - V_{606}) < 1.2 \text{ mag} \\ \text{and } (B_{435} - V_{606}) > -0.2 \text{ mag} \\ \text{and } (U_{336} - B_{435}) > 0.35 + [1.3 \times (B_{435} - V_{606})] \text{ mag} \\ \text{and } [S/N(B_{435})] > 3, [S/N(U_{336})] < 3, [S/N(U_{275})] < 1, [S/N(U_{225})] < 1 \end{array} \right.$$

We require $(U_{336} - B_{435}) > 0.8$ mag, which is bluer than what we have applied for other dropouts, because we have two bands bluer than U_{336} to confirm that these dropouts are not detected ($S/N < 1$) at wavelengths bluer than rest-frame 912 Å. There are 1156 objects inside the selection region. We find a total of 260 LBG candidates (U_{336} -dropouts) based on the above mentioned selection criteria. After visually checking each candidate, we eliminated 4 spurious candidates (same reason as discussed before for other dropout candidates). The final sample consists of 256 U_{336} -dropouts.

The gray data points in the bottom panels of Figure 2 shows *all* the sources in our catalogs that are not selected as LBG candidates. Those that fall within our selection regions were excluded from our candidate samples mainly because of our low S/N cuts (< 1) in the bluer bands and the hard magnitude limit (< 26.5 mag) in the selection band. The primary reason for this is the varying depth of these filters. The B_{435} is much deeper than U_{336} , so when we select U_{336} -dropouts with $B_{435} < 26.5$ mag, we are not selecting galaxies fainter than 26.5 mag in B_{435} . We cannot conclusively say whether these faint galaxies are LBG candidates or not because of the shallower U_{336} images. Similarly, U_{225} and U_{275} are slightly deeper than U_{336} , so while selecting the U_{275} - or U_{336} -dropouts, our selection criteria of $S/N < 1$ in the bluer bands still keeps some faint objects (with $S/N > 1$) in the selection region which are not selected as dropouts. Therefore, the varying depth between filters, combined with our magnitude and S/N cuts, are responsible for objects in the selection region that are not selected as LBG candidates. Overall, our selection is conservative, because of these constraints.

There are a few compact objects in our selected samples, but when we visually check these objects in the 10-band HST imaging, and compare with the more robustly selected star catalog of Windhorst et al. (2010), we cannot confirm any stars. Windhorst et al. (2010) gives a detailed discussion of the star-galaxy separation procedure used for the ERS2 data, and confirms that within our sample magnitude range (24–26.5 mag) there are practically no stars in the UV bands, and very few in the B-band. There could be a weak AGN in some of these galaxies, which we will investigate in our future paper on stellar populations and spectral analysis of these LBGs.

Figure 3 shows three example images of color selected UV-dropouts whose redshifts are

confirmed by ground-based spectroscopy (see next section). These examples are shown here in the 10-band HST imaging obtained from ERS2 observations. The final sample consists of 66 U_{225} -, 151 U_{275} - and 256 U_{336} -dropouts. There is one object overlapping between U_{225} - and U_{275} -dropout samples, while seven objects are in common between U_{275} - and U_{336} -dropout samples.

2.2. Reliability of Color Selection

In order to test reliability of our color selection, we compare our dropout samples with spectroscopic redshifts from the Very Large Telescope (VLT; e.g., Grazian et al. 2006; Wuyts et al. 2008; Vanzella et al. 2008; Balestra et al. 2010) and with the 10-band (3 WFC3 UV, 4 ACS optical and 3 WFC3 IR) photometric redshifts obtained from our ERS2 observations (Cohen et al. 2010, in prep). When we match our dropout catalogs with these redshift catalogs, we find that $\sim 80\%$ of our dropouts have photometric redshifts, but only $\sim 30\%$ have spectroscopic redshifts. Though photometric redshifts are from the same ERS2 dataset, we don't have 100% matching catalogs. The ERS2 photometric redshifts are based on the H_{160} -band selected catalogs, and the WFC3 IR channel covers a smaller area than the WFC3 UVIS or ACS/WFC cameras, which were used here to identify these UV dropouts. The most likely reason for the low number of spectroscopic confirmations is the ‘redshift desert’. The galaxies in this redshift range ($1 \lesssim z \lesssim 3$) are difficult to identify via ground-based spectroscopy, because of the lack of strong features in 4500–9000 Å range, where most spectrographs on large telescopes are optimized.

Figure 4 shows the redshift distributions of the dropout LBG candidates — three dropout samples are shown in three separate panels — with spectroscopic and photometric redshifts. The hashed (solid gray) histogram and solid (dot-dash) curve shows the distribution and the best Gaussian fit to the number of LBG candidates with photometric (spectroscopic) redshifts. Table 1 lists the number of dropouts with spectroscopic/photometric redshifts and their average redshifts obtained from the distributions in Figure 4.

Figure 4 shows that based on these available redshifts, our dropout selection is very reliable, and that WFC3 UV filters provide a very efficient way to select LBGs at $z \simeq 1–3$. Spectroscopic redshifts are only available for $\sim 30\%$ of our dropout galaxies, and have — on average — $\sim 6\%$ outliers or low- z interlopers ($\sim 5\%$ for U_{225} -, $\sim 5\%$ for U_{275} - and $\sim 9\%$ for U_{336} -dropouts). The outliers are defined as any object at $z \lesssim 1$. The ERS2 photometric redshifts are available for $\sim 80\%$ of our dropouts and have — on average — $\sim 12\%$ outliers with the most ($\sim 15\%$) amongst the U_{225} -dropouts, as expected because of the lack of any available WFC3 bands bluer than U_{225} . The comparison of our color selected dropouts

with spectroscopic and photometric redshifts show that the fraction of outliers in both cases are comparable or better than the fraction of outliers in spectroscopic follow-up surveys of star-forming galaxies and dropout selected LBGs at $z \simeq 1.5 - 3.4$, which is about $\sim 5\text{--}15\%$ (Steidel et al. 2003, 2004; Reddy et al. 2008; Ly et al. 2009). A similar comparison with publicly available photometric redshifts (e.g., Wuyts et al. 2008; Santini et al. 2009) shows that they have a higher percentage of outliers ($\sim 17\%$), because these large surveys have mostly shallow ground-based near-UV data which cannot go bluer than $\sim 3000 \text{ \AA}$, because of the atmospheric cut-off. Therefore, space-based WFC3 UV data are essential to get accurate photometric redshifts for these lower redshift galaxies ($z \simeq 1 - 3$).

The average spectroscopic or photometric redshift for U_{336} -dropouts from Figure 4 is $z \simeq 2.4$, but based on the location of the Lyman break (Figure 1), the average redshift for U_{336} -dropouts should be about $z \sim 3.0$. We have identified small number of brighter ($\lesssim 26.0$ mag) LBG candidates at $z \gtrsim 2.8$, but we are missing a significant number of fainter (> 26.0 mag) LBG candidates at these redshifts. The main reason is that we require redder colors ($U_{336} - B_{435} \gtrsim 2.0$ mag) to select higher redshift galaxies in this dropout sample, because the Ly α forest absorption at 912-1216 \AA begins to increasingly affect the U_{336} band at these redshifts. This implies that we need the U_{336} images to be $\sim 1\text{--}1.5$ mag deeper to consistently select all dropouts at $z \gtrsim 2.8$, improve the photometric redshift distribution, and lower the number of outliers for this sample. Therefore, we have a relatively smaller number of LBG candidates (within our magnitude limit) at $z \gtrsim 2.8$ in the U_{336} -dropouts sample.

3. Results and Discussion

3.1. Number Counts

The observed raw number counts of LBG candidates at $z \simeq 1 - 3$ at a rest-frame wavelength of 1700 \AA are shown in Figure 5. When we combine all three dropout samples, the average photometric redshift is $z \simeq 2.2$. For proper comparison, these number counts are *not* corrected for incompleteness or cosmic variance, and therefore, the counts start to drop at fainter magnitudes ($\gtrsim 26.0$ mag). Figure 5 (top panel) shows number counts (in number per arcmin^2 per 0.5 mag bin) of *all* dropouts ($z \simeq 1 - 3$) in our sample compared with other ground-based and space-based LBG surveys (Steidel et al. 1999; Nonino et al. 2009; Ly et al. 2009) at $z \simeq 2 - 3$. We have also plotted $z \simeq 4 - 6$ number counts from Bouwens et al. (2007) to show the change in the surface densities (number per arcmin^2) as a function of redshift.

Steidel et al. (1999, $z \simeq 3$) used ground-based imaging in ~ 14 fields, with each field observed for many kilo-seconds (ks), followed by ground-based spectroscopy to confirm many

of their color selected candidates. The Steidel et al. (1999) selection was based on LBG color criteria down to AB \sim 25 mag. Nonino et al. (2009) observed the GOODS-South field using VLT/VIMOS to get deep U -band imaging (AB \sim 27 mag). Their number counts for LBG candidates at $z \simeq 3$ shown in Figure 5 come from the deepest part of the VIMOS field, which covers \sim 88 arcmin 2 with exposure time of \sim 20 hours (72 ks). On the other hand, Ly et al. (2009) observed the Subaru Deep Field (Kashikawa et al. 2004) using deep (>100 ks) near-UV imaging from the space-based GALEX observations (with \sim 5" FWHM resolution) to select LBG candidates at $z \simeq 2.2$ down to AB \sim 25 mag, and used ground-based spectroscopy to confirm many LBGs at $z \simeq 2.2$.

From Figure 5 (top panel) we note three major points. First, there is only one space-based — GALEX — LBG survey at $z \simeq 2.2$ (Ly et al. 2009), which clearly shows that the WFC3 UV observations — with better sensitivity and resolution — can play a vital role in identifying LBGs at $z \lesssim 2.5$. Secondly, all surveys mentioned above use deep UV imaging with $\gtrsim 70$ ks exposures, while our WFC3 UV observations are only $\lesssim 5$ ks (1 to 2 orbits), and still we find that our observations are \sim 0.5–1.0 mag deeper compared to some of these surveys. Finally, our numbers agree very well with the decreasing trend of LBG surface densities as a function of redshift from $z \simeq 2.0$ to 6.0, which we will address quantitatively in the next section.

The bottom panel of Figure 5 shows number counts for each dropout sample. The U_{275} - and U_{336} -dropout samples show comparable number counts and agree generally with surveys at higher redshifts, but the U_{225} -dropouts show lower number counts. Given the trend with redshift shown by other samples in the upper panel of Figure 5, we would expect more U_{225} -dropouts than other dropouts at higher redshifts. The numbers are smaller than expected because of the conservative selection criteria we applied owing to the absence of a second filter below the Lyman break (see § 2.1) to confirm our dropout selection. This approach led us to small numbers of U_{225} -dropouts in a relatively narrow redshift range around $z \simeq 1.7$. Hence, we don't have a fully representative U_{225} -dropout sample, but with the future deeper observations we can use a somewhat more liberal selection criteria to get better statistics for this sample.

3.2. Determination of the UV Luminosity Function

We calculated the rest-frame UV luminosity functions (LF) using the V_{eff} method (e.g., Steidel et al. 1999; Sawicki & Thompson 2006; Ly et al. 2009) in 0.5 mag wide bins. The absolute magnitudes of LBG candidates were measured in the observed bands that are equivalent to rest-frame 1500 Å to minimizes k -corrections, and using the average redshift

for each object in each sample ($z \simeq 1.7, 2.1, 2.7$, respectively). These absolute magnitudes are uncorrected for internal dust absorption.

We compute LFs for the three dropout samples: U_{225} -dropouts ($z \simeq 1.7$ LBG candidates), U_{275} -dropouts ($z \simeq 2.1$ LBG candidates), and U_{336} -dropouts ($z \simeq 2.7$ LBG candidates). Figure 6 shows the LFs for these three dropout samples. We model these LFs with a standard Schechter function (Schechter 1976), which is parametrized by the characteristic absolute magnitude (M^*), the normalization (ϕ^*), and the faint-end slope (α). The shaded gray regions in Figure 6 show the uncertainty in the LF based on $1-\sigma$ uncertainty in M^* and α . Table 2 lists the best-fit Schechter function parameters M^* , α and ϕ^* for these three dropout samples.

To investigate incompleteness in each redshift bin, we ran simulations to calculate $P(m, z)$, which is the probability that a galaxy of apparent magnitude m and at redshift z will be detected in the image *and* will meet our color selection criteria. In these simulations, large numbers of artificial objects with a range of redshifts and magnitudes were added to the real ERS2 images, and then recovered using exactly the same method and selection criteria that were employed for the real observations. For these simulations, we used BC03 models assuming Salpeter Initial Mass Function (IMF), constant SFR, solar metallicity, $E(B - V) = 0.0 - 0.3$, an age of 1 Gyr with different redshift range for each sample and varying magnitudes. These models were used to generate color and extinction properties of our artificial objects. We chose artificial objects to be point-like sources. The selection function obtained from this exercise (adding and recovering artificial objects) is similar in shape as the distributions in Figure 4, and the mean redshift value obtained from these simulations (for each sample) is within 1-sigma of the mean value obtained in Figure 4. These $P(m, z)$ estimates were used to determine V_{eff} for the LF.

We did not make the corrections for interlopers in our LF estimates. There are five main reasons for this. First, we have checked our LFs by boosting the errors by 10%, and we find that the best fit values remain the same, while the uncertainties on these values increases slightly. Second, the limited number of spectroscopic redshifts ($\lesssim 30\%$ candidates have spectroscopic redshifts) does not give us a correct estimate of interlopers in our color selected sample. Third, the total fraction of spectroscopic interlopers is very small ($\lesssim 9\%$), and when we subdivide them as a function of magnitude it is even smaller. Fourth, the estimate of interlopers based on photometric redshifts is not very accurate because of uncertainty in the photometric redshifts. Though the ERS2 photometric redshifts (Cohen et al. 2010, in prep) are better than some of the publicly available photometric redshifts, they are still uncertain by a few percent. Finally, for the U_{275} - and U_{336} -dropouts the faintest bin is most affected by the interlopers, but that data point is already uncertain because of very few objects in

that bin.

3.2.1. Luminosity Functions

The leftmost panel of Figure 6 shows the resulting LF for U_{225} -dropouts. The three brightest bins contain on average 3 objects per bin, and hence they are more uncertain. That leaves us with only three data points with a statistically significant number of objects. It is not possible to fit a Schechter function to three data points by keeping all three parameters free. In the absence of deeper data, we fix the faint-end slope, α , based on the best-fit observed trend between redshifts and α for LBGs at $z \simeq 1.5 - 8$ (Figure 7). The best-fit parameters for this dropout sample are meant to be mostly illustrative due to low number statistics. The middle panel of Figure 6 shows the LF for the U_{275} -dropouts and the rightmost panel shows the LF for the U_{336} -dropouts. It is difficult to estimate the faint-end slope from these observations, as we can see from the uncertain faintest point in the LFs of U_{275} - and the U_{336} -dropouts. Though our best-fit estimates are very close to what we expect at these redshifts ($z \simeq 1 - 3$) from other studies (e.g., Steidel et al. 1999; Ly et al. 2009) at nearby redshifts, we will need deeper ($\sim 1 - 2$ mag) UV observations to properly constrain the faint-end slope for these three dropout samples.

3.2.2. Redshift Evolution of M^* and α

In general, it is not straightforward to directly compare our LFs with those from previous studies. First, our redshift range is different, and this is the first time that this camera and filter set have been used to select LBGs. Secondly, in some cases the adopted cosmologies are slightly different. It is well known (e.g., Sawicki & Thompson 2006) that the derived LFs strongly depends on the assumed cosmological models, but the evolutionary trends seen in the LFs in our three redshift bins are virtually independent of the assumed cosmology. Figure 7 shows the evolutionary trends in our three redshift bins, as well as comparisons to other studies on LBGs at different redshifts.

The top panel of Figure 7 shows the faint-end LF slope, α , as function of redshift. The Arnouts et al. (2005) $z \lesssim 1.5$ sample is based on the spectroscopically confirmed galaxies with the GALEX near-UV detection ($\lesssim 24.5$ mag), and the $z > 1.5$ sample is based on the photometric redshifts. The Arnouts et al. (2005) samples are not selected based on Lyman break color criteria but because of the lack of LBG candidates at $z \lesssim 2.0$, we have used this star-forming galaxies sample for comparison. The Reddy & Steidel (2009) and the Ly et al.

(2009) samples are dropout selected LBGs at $z \simeq 3$ and $z \simeq 2.2$, respectively. The black line is the best-fit observed trend between α and z for LBGs at $z \simeq 1.5–8$, which is very similar to that of Ryan et al. (2007). The observed trend is that as the redshift increases, the faint-end slope, α , becomes steeper (more negative), illustrating that lower luminosity dwarf galaxies dominate the galaxy population at higher redshifts. Excluding the fixed α data point at $z \simeq 1.7$, our data points at $z \simeq 2.1$ and $z \simeq 2.7$ agree very well — within the current uncertainties — with the black line, as well as with other data points in close redshift proximity.

The bottom panel of Figure 7 shows the characteristic absolute magnitude, M^* , as a function of redshift. Again, the general observed trend is that as redshift increases, the characteristic absolute magnitude, M^* , becomes brighter (more negative) until $z \simeq 3.5$. This trend is considered as an evidence of ‘downsizing’ galaxy formation scenario (e.g., Cowie et al. 1996), where luminous massive galaxies form at higher redshifts. Our first data point at $z \simeq 1.7$ follows this general trend, but it is more uncertain due to the limited statistics in this dropout sample. The other two data points at $z \simeq 2.1$ and 2.7 fit very well within the evolutionary trend seen at these and higher redshifts. Figure 7 shows rapid decline of M^* between $z \simeq 3$ and extending to $z \simeq 1.5$. This turnover is well defined in our and Ly et al. (2009) samples. It is important for future surveys to exploit the special capabilities of the WFC3 in the near-UV to obtain larger samples to understand the relation between this critical transition in M^* and physical processes in LBGs at $z < 3$.

Reddy & Steidel (2009) have used deep ground-based imaging data to constrain the UV LF of the ‘BX’ (e.g., Adelberger et al. 2004) population at $1.9 < z < 2.7$, which selects star-forming galaxies based on U_nGR colors. When we compare our LFs with that of the ‘BX’ population, we find some differences in M^* and α values. First, our U_{225} -dropout sample has lower redshift ($z \sim 1.7$) compared to the ‘BX’ population ($z \sim 2.3$), so our M^* value (-19.43 mag) is fainter than their value of -20.70 mag, and agrees with the general trend discussed above. Second, M^* values of our U_{275} -dropout sample and the ‘BX’ sample agree within our $1-\sigma$ uncertainty, while the α is little steeper for the ‘BX’ sample. We believe that complete agreement between our LBGs sample and the ‘BX’ sample is not possible, because although the ‘BX’ selection selects star-forming galaxies, it is very likely that the dropout selected sample at a similar redshift might not be same as the ‘BX’ selected sample. Some galaxies which are selected through the ‘BX’ color selection criteria might not be in the dropout selected sample, and vice versa. Therefore, it is difficult to directly compare the ‘BX’ and the LBG samples, and the differences in these samples could cause the LF parameters at similar redshift to differ (see also Ly et al. 2009).

Therefore, for both M^* and α our results agree very well with the expected observed

trends (Figure 7) as a function of redshift. At lower redshifts ($z < 3$), our data points will help to reduce the gap between the well studied $z \gtrsim 3$ and $z \sim 0$ regimes. The agreement with the observed evolutionary trend of M^* and α also show the reliability of our LFs, which can be improved with the future deeper and wider WFC3 UV observations (e.g., CANDELS Multi-Cycle Treasury program # 12060-12064, PI: S. Faber).

4. Summary

We use newly acquired UV observations from the WFC3 UVIS channel along with existing deep ACS observations of the GOODS program, to identify UV dropout galaxies, which are LBG candidates at $z \simeq 1-3$. We find 66 U_{225} -, 151 U_{275} - and 256 U_{336} -dropouts to a magnitude limit of $AB \simeq 26.5$ mag. This allows us to estimate rest-frame UV LFs in three redshift bins ($z \simeq 1.7, 2.1, 2.7$). Their best-fit Schechter function parameters M^* , α and ϕ^* agree very well with the observed evolution of these parameters with respect to redshift. We need space-based UV imaging to identify and understand the $z \lesssim 3$ LBGs selected based on their UV dropout signature. The new WFC3 UVIS camera on the HST now allows us to do that with much better sensitivity and resolution than GALEX, and has opened up a new regime of detailed UV imaging studies of low to intermediate redshift ($z \lesssim 3$) LBGs, which is not possible from the ground due to the atmospheric cut-off. The quality of rest-frame near-UV imaging ($\gtrsim 3000 \text{ \AA}$) of these galaxies greatly exceeds that which can be done with ground-based near-UV observations. Future work will investigate the morphology and stellar populations of these lower redshift LBGs, to better understand their higher redshift counterparts. The upcoming WFC3 UVIS imaging surveys — deep and wide — have the potential to robustly measure the evolution of LBGs at $z \lesssim 3$, and — with uniform selection all-the-way to very high redshifts — provide better understanding of very high redshift LBGs.

We thank the referee for helpful comments and suggestions that significantly improved this paper. We thank M. Nonino, C. Ly and their collaborators for providing their LBG number counts. This paper is based on Early Release Science observations made by the WFC3 Scientific Oversight Committee. We are grateful to the Director of the Space Telescope Science Institute for awarding Director’s Discretionary time for this program. Finally, we are deeply indebted to the brave astronauts of STS-125 for rejuvenating HST. Support for program #11359 was provided by NASA through a grant from the Space Telescope Science Institute, which is operated by the Association of Universities for Research in Astronomy, Inc., under NASA contract NAS 5-26555.

REFERENCES

Adelberger, K. L., Steidel, C. C., Shapley, A. E., et al. 2004, ApJ, 607, 226

Arnouts, S., Schiminovich, D., Ilbert, O., et al. 2005, ApJ, 619, L43

Balestra, I., Mainieri, V., Popesso, P., et al. 2010, A&A, 512, A12

Bertin, E., & Arnouts, S. 1996, A&AS, 117, 393

Bouwens, R. J., Illingworth, G. D., Franx, M., & Ford, H. 2007, ApJ, 670, 928

Bouwens, R. J., Illingworth, G. D., Oesch, P. A., et al. 2010a, ApJ, 709, L133

Bouwens, R. J., Illingworth, G. D., Oesch, P. A., et al. 2010b, ApJ, submitted
(arXiv:1006.4360)

Bruzual, G., & Charlot, S. 2003, MNRAS, 344, 1000

Bunker, A. J., Wilkins, S., Ellis, R., et al. 2010, MNRAS, in press (arXiv:0909.2255)

Coleman, G. D., Wu, C.-C., & Weedman, D. W. 1980, ApJS, 43, 393

Cowie, L. L., Songaila, A., Hu, E. M., & Cohen, J. G. 1996, AJ, 112, 839

Dickinson, M., Stern, D., Giavalisco, M., et al. 2004, ApJ, 600, L99

Giavalisco, M., Ferguson, H. C., Koekemoer, A. M., et al. 2004a, ApJ, 600, L93

Giavalisco, M., Dickinson, M., Ferguson, H. C., et al. 2004b, ApJ, 600, L103

Grazian, A., Fontana, A., de Santis, C., et al. 2006, A&A, 449, 951

Guhathakurta, P., Tyson, J. A., & Majewski, S. R. 1990, ApJ, 357, L9

Kalirai, J. S., MacKenty, J., Rajan, A., et al. 2009, Instrument Science Report WFC3 2009-31

Kashikawa, N., Shimasaku, K., Yasuda, N., et al. 2004, PASJ, 56, 1011

Kinney, A. L., Calzetti, D., Bohlin, R. C., et al. 1996, ApJ, 467, 38

Koekemoer, A. M., Fruchter, A. S., Hook, R. N., & Hack, W. 2002, The 2002 *HST* Calibration Workshop, ed. S. Arribas, A. Koekemoer, and B. Whitmore (Baltimore:STScI), 337

Komatsu, E., Dunkley, J., Nolta, M. R., et al. 2009, ApJS, 180, 330

Labbé, I., González, V., Bouwens, R. J., et al. 2010, ApJ, 708, L26

Ly, C., Malkan, M. A., Treu, T., et al. 2009, ApJ, 697, 1410

Nonino, M., Dickinson, M., Rosati, P., et al. 2009, ApJS, 183, 244

Madau, P. 1995, ApJ, 441, 18

Oesch, P. A., Bouwens, R. J., Illingworth, G. D., et al. 2010, ApJ, 709, L16

Oke, J. B., & Gunn, J. E. 1983, ApJ, 266, 713

Pickles, A. J. 1998, PASP, 110, 863

Rafelski, M., Wolfe, A. M., Cooke, J., et al. 2009, ApJ, 703, 2033

Reddy, N. A., Steidel, C., Pettini, M., et al. 2008, ApJS, 175, 48

Reddy, N. A., & Steidel, C. C. 2009, ApJ, 692, 778

Ryan, R. E., Hathi, N. P., Cohen, S. H., et al. 2007, ApJ, 668, 839

Santini, P., Fontana, A., Grazian, A., et al. 2009, A&A, 504, 751

Sawicki, M., & Thompson, D. 2006, ApJ, 642, 653

Schechter, P. 1976, ApJ, 203, 297

Stark, D. P., Ellis, R. S., Chiu, K., et al. 2010, MNRAS, submitted (arXiv:1003.5244)

Steidel, C. C., Giavalisco, M., Pettini, M., et al. 1996, ApJ, 462, L17

Steidel, C. C., Adelberger, K. L., Giavalisco, M., et al. 1999, ApJ, 519, 1

Steidel, C. C., Adelberger, K. L., Shapley, A. E., et al. 2003, ApJ, 592, 728

Steidel, C. C., Shapley, A., Pettini, M., et al. 2004, ApJ, 604, 534

Vanzella, E., Cristiani, S., Dickinson, M., et al. 2008, A&A, 478, 83

Windhorst, R. A., Cohen, S. H., Hathi, N. P., et al. 2010, ApJS, submitted (arXiv:1005.2776)

Wuyts, S., Labbé, I., Schreiber, N. M. F., et al. 2008, ApJ, 682, 985

Yan, H., Windhorst, R. A., Hathi, N. P., et al. 2010, RAA, in press (arXiv: 0910.0077)

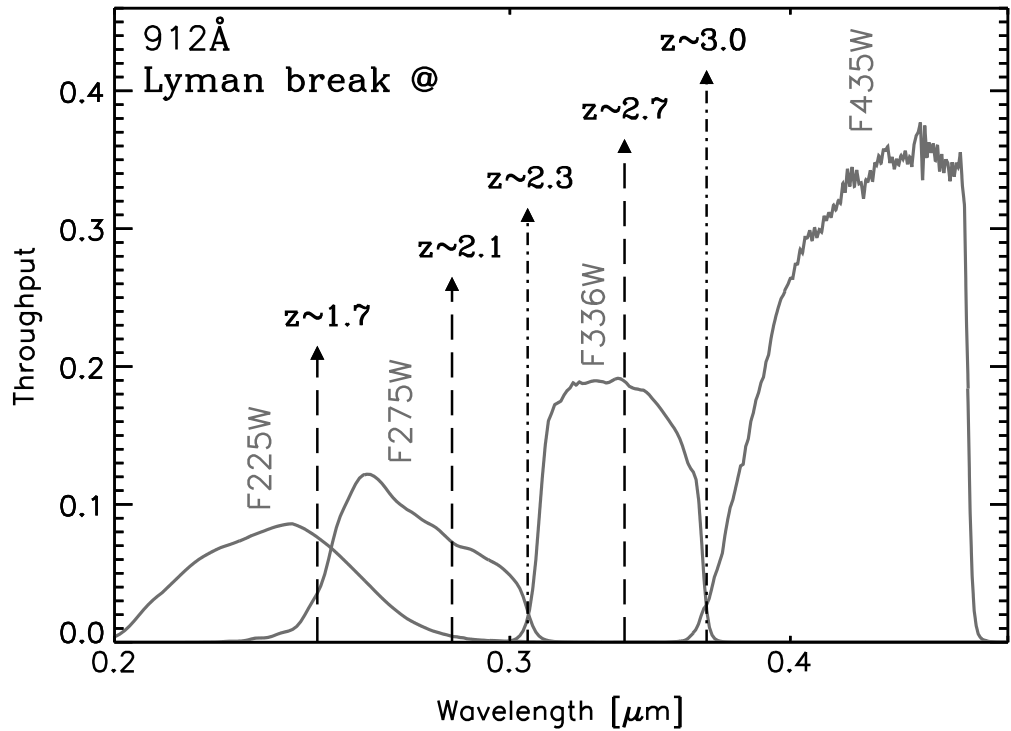


Fig. 1.— Rest-Frame 912 Å Lyman break at different redshifts is shown with filter transmission curves of three WFC3 UVIS filters and the B_{435} -band ACS optical filter. It is evident that $z \simeq 1-3$ LBG candidates can be efficiently selected using these three WFC3 UV filters.

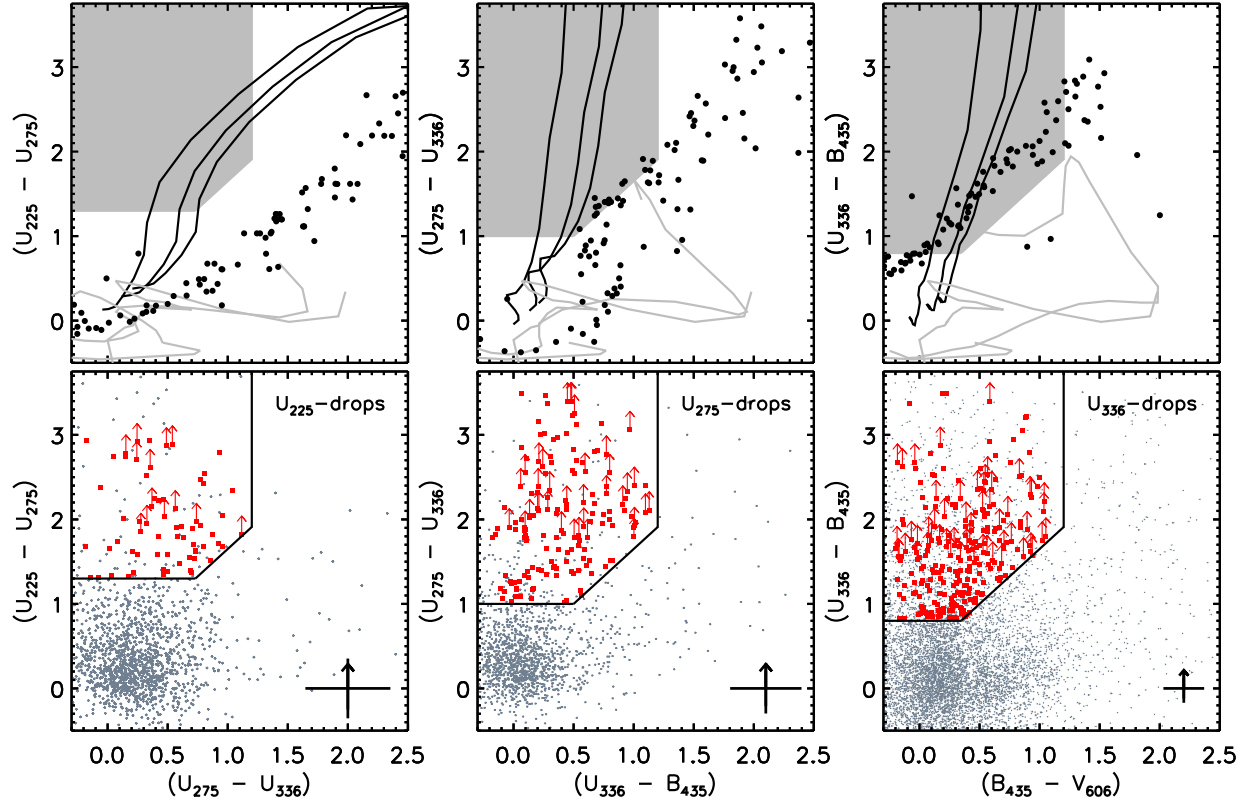


Fig. 2.— The top three panels show color selection region (gray shaded region) obtained using BC03 star-forming galaxy models with $E(B-V) = 0, 0.15, 0.30$ mag (solid black lines), expected colors of stars (black dots) from Pickles (1998), and tracks of low-redshift ellipticals (gray lines) from Kinney et al. (1996) and Coleman et al. (1980). Though stars clearly land in the selection region, these are easily removed by simple morphological criteria, as in Windhorst et al. (2010). [Bottom-Left] shows the color-color plot with the U_{225} -dropout selection region, [Bottom-Middle] shows the selection of the U_{275} -dropouts and [Bottom-Right] shows the selection of the U_{336} -dropouts. The gray data points in the bottom panels are *all* objects in the catalog. Average uncertainties in the color measurements are shown as the error bar in the lower right corner. Red points indicate the selected dropouts, while gray data points in the selected region were excluded by other criterion as given in § 2.1.

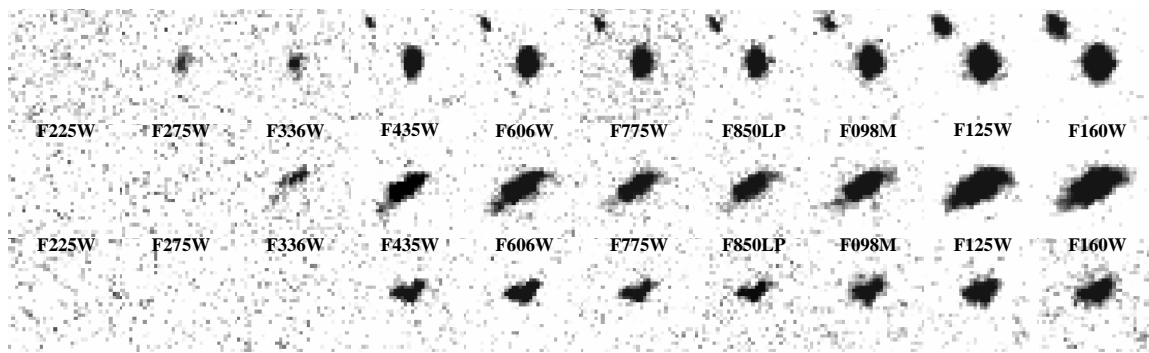


Fig. 3.— Three examples of color selected UV-dropouts with spectroscopic redshifts are shown here in the 10-band HST imaging from the ERS2 data. The object at the top is a U_{225} -dropout ($V_{606} \sim 24.5$ mag) with a spectroscopic redshift of $z \simeq 1.61$, the object in the middle is a U_{275} -dropout ($V_{606} \sim 23.9$ mag) with $z \simeq 2.04$, and the object at the bottom is a U_{336} -dropout ($V_{606} \sim 24.7$ mag) with $z \simeq 2.69$. Each stamp is 3'' on a side, has North up, and has a pixel scale of 0.09''/pixel.

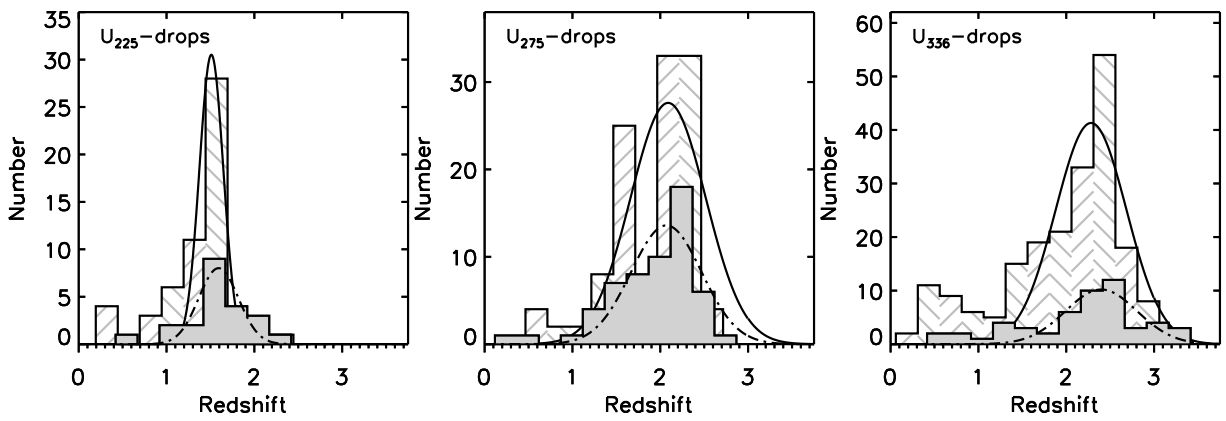


Fig. 4.— The hashed histogram (solid gray) and solid (dot-dash) curve shows the distribution and the Gaussian fit, respectively, to our LBG candidates with photometric (spectroscopic) redshifts. [Left] shows distribution of 55 (22) U_{225} -dropouts with photometric (spectroscopic) redshifts. The average redshifts are $\langle z_{ph} \rangle = 1.51 \pm 0.13$ and $\langle z_{sp} \rangle = 1.59 \pm 0.22$, [Middle] shows the distribution of 117 (57) U_{275} -dropouts with photometric (spectroscopic) redshifts. The average redshifts are $\langle z_{ph} \rangle = 2.09 \pm 0.42$ and $\langle z_{sp} \rangle = 2.07 \pm 0.40$, and [Right] shows the distribution of 203 (52) U_{336} -dropouts with photometric (spectroscopic) redshifts. The average redshifts are $\langle z_{ph} \rangle = 2.28 \pm 0.40$ and $\langle z_{sp} \rangle = 2.40 \pm 0.40$.

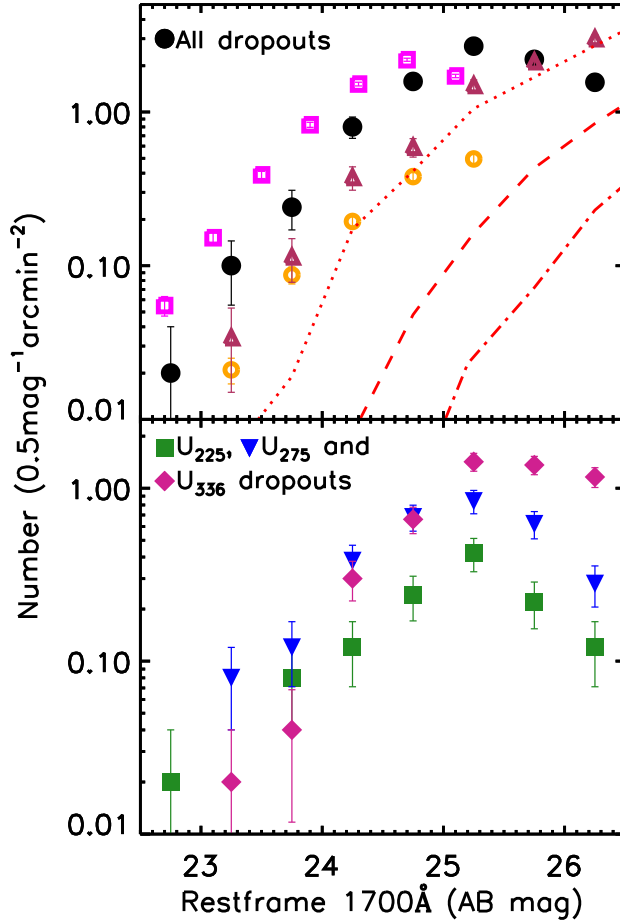


Fig. 5.— [Top] Rest-frame 1700 Å number counts (i.e., number per arcmin² per 0.5 mag bin) of all dropouts ($z \simeq 1-3$) in our sample shown by black solid circles, along with the studies of Steidel et al. (1999, $z \simeq 3$, orange open circles), Nonino et al. (2009, $z \simeq 3$, maroon open triangles) and Ly et al. (2009, $z \simeq 2.2$, magenta open squares). The red lines are the number counts from Bouwens et al. (2007) for LBGs at $z \simeq 4$ (dotted), $z \simeq 5$ (dashed) and $z \simeq 6$ (dot-dash). [Bottom] The bottom panel shows our number counts for each dropout sample (U_{225} , U_{275} , U_{336}). The vertical error bars in our data are 1σ Poisson uncertainties.

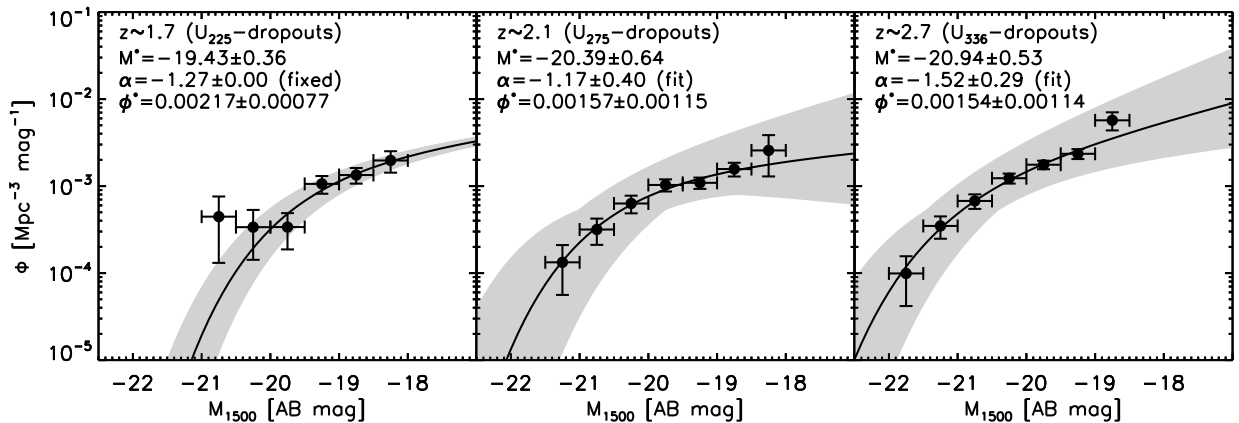


Fig. 6.— Rest-frame UV luminosity functions for $z \simeq 1-3$. The best fit Schechter function parameters are shown for each LF. The gray shaded region shows uncertainty in the LF based on $1-\sigma$ uncertainties in α and M^* . In the leftmost panel, α is kept fixed while fitting the Schechter function, so the uncertainty indicated with the gray shaded region is based on $1-\sigma$ uncertainty of M^* only. The more uncertain brightest point in the leftmost panel occurs because of very limited statistics and does not contribute to the best fit parameters, while the uncertain faintest points in the middle and the rightmost panel are at the limit of our observations, and could also be affected by low redshift interlopers. The vertical error bars in our data are 1σ Poisson uncertainties.

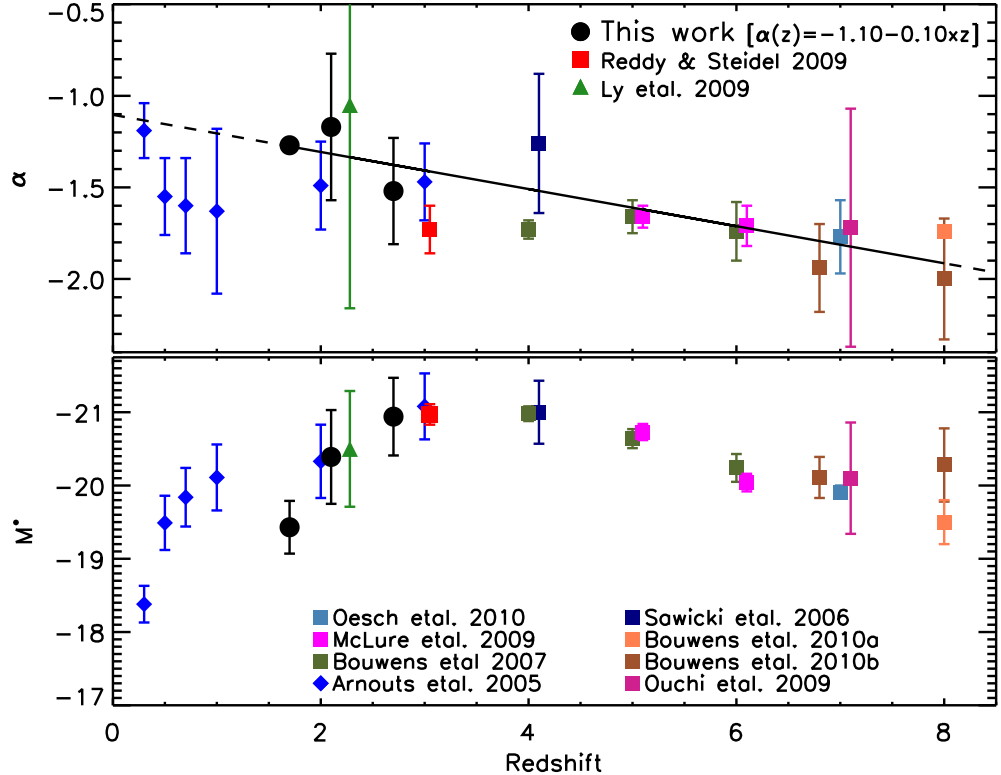


Fig. 7.— The best fit Schechter function parameters at rest-frame far-UV wavelengths — the faint-end slope α (top panel) and the characteristic absolute magnitude M^* (bottom panel) — as a function of redshift. The solid black line in the top panel is the best fit $\alpha-z$ relation for LBGs at $z \simeq 1.5-8$ and extended on both sides by the dashed line. The $z \simeq 1.7$ α value is fixed because not enough data was available to fit it. The Arnouts et al. (2005) $z \lesssim 1.5$ sample is based on the spectroscopically confirmed galaxies with the GALEX near-UV detection, and the $z > 1.5$ sample is based on the photometric redshifts. The Reddy & Steidel (2009) and the Ly et al. (2009) samples are dropout selected LBGs at $z \simeq 3$ and $z \simeq 2.2$, respectively. The data points at $z \simeq 3-8$ are for LBGs at high redshift. Our results (black filled circles) agree very well with the general evolutionary trend observed for both these parameters.

Table 1. Number and Redshifts of UV-dropouts in the ERS2 field

Dropout Filter	Total Number of Candidates	No. of Spectroscopic Redshifts ^a and $\langle z \rangle^c$	No. of Photometric Redshifts ^b and $\langle z \rangle^c$
U_{225}	66	22 1.59 ± 0.22	55 1.51 ± 0.13
U_{275}	151	57 2.07 ± 0.40	117 2.09 ± 0.42
U_{336}	256	52 2.40 ± 0.40	203 2.28 ± 0.40

^aFrom compilation of VLT redshifts (e.g., Grazian et al. 2006; Wuyts et al. 2008; Vanzella et al. 2008; Balestra et al. 2010)

^bFrom Cohen et al. 2010, in prep.

^cFrom the Gaussian fit to the distribution shown in Figure 4

Table 2. Parameters of Schechter Function Fits

Dropout Filter	M^* (1500 Å) (AB mag)	ϕ^* $\text{mag}^{-1} \text{Mpc}^{-3}$	α
U_{225}	-19.43 ± 0.36	0.00217 ± 0.00077	-1.27 (fixed)
U_{275}	-20.39 ± 0.64	0.00157 ± 0.00115	-1.17 ± 0.40
U_{336}	-20.94 ± 0.53	0.00154 ± 0.00114	-1.52 ± 0.29